

# DEMOGRAPHIC-AWARE FINE-GRAINED CLASSIFICATION OF PEDIATRIC WRIST FRACTURES

Ammar Ahmed<sup>1</sup>, Ali Shariq Imran<sup>1,\*</sup>, Zenun Kastrati<sup>2</sup>, Sher Muhammad Daudpota<sup>3</sup>

<sup>1</sup> Department of Computer Science (IDI), Norwegian University of Science & Technology (NTNU), Gjøvik, 2815, Norway

<sup>2</sup> Department of Informatics, Linnaeus University, Växjö, 351 95, Sweden

<sup>3</sup> Department of Computer Science, Sukkur IBA University, Sukkur, 65200, Pakistan

## ABSTRACT

Wrist pathology recognition from radiographs is challenging because normal appearance varies markedly with age and sex. In pediatric imaging, evolving carpal ossification and open growth plates can resemble fractures, while sex-dependent timing of physal closure changes key visual cues. Image-only models therefore risk confusing developmental anatomy for pathology, especially in small medical datasets. We address this by framing wrist diagnosis as a fine-grained visual recognition (FGVR) task and introducing a multimodal transformer that fuses X-rays with demographic metadata (age and sex). Unlike prior work, this is the first study to integrate metadata for wrist pathology recognition, and we further show that fine-grained pretraining transfers better than coarse ImageNet initialization. Our approach improves accuracy by 2% on a small curated dataset and by over 10% on a larger fracture dataset.

**Index Terms**— Pediatric fractures, fracture detection, X-rays, fine-grained classification, Patient metadata

## 1. INTRODUCTION

Wrist fractures represent up to 75% of hand injuries in emergency departments and pose a significant risk of long-term impairment if misdiagnosed [1]. Given the wrist’s complex anatomy and developmental variability, accurate radiographic interpretation is essential. Recent advances in computer vision have demonstrated promise for automated abnormality detection in musculoskeletal imaging. However, such methods typically rely on large, labeled datasets, which are scarce in medical domains, and often process X-rays without contextual patient information.

To overcome the limitations of image-only learning, multimodal frameworks that fuse patient metadata with imaging have been successfully applied in dermatology and oncology. Studies have shown consistent accuracy improvements by incorporating age, sex, and anatomical site information alongside dermoscopic or histopathology images. For example, Thomas et al. [2] fused demographic variables with der-

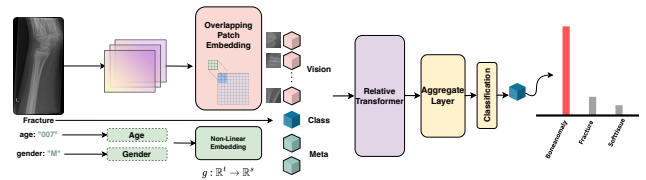


**Fig. 1:** The architecture pipeline integrates visual, class, and meta tokens within a transformer framework.

mography images, while Cai et al. [3] applied ViTs with metadata encoders, achieving 93.8% melanoma classification accuracy. Recently, Hinterwimmer et al. [4] extended this approach to musculoskeletal imaging, reporting gains in bone tumour classification by integrating X-rays and metadata.

Despite these advances, metadata integration has not been investigated for wrist pathology recognition. This gap is significant, as age- and sex-specific skeletal variations critically influence wrist imaging. Carpal ossification follows predictable stages, growth plate closure occurs at different ages across sexes [5, 6], and pediatric fracture types differ from adult patterns [7]. Without demographic context, models may misclassify normal developmental features, such as unfused growth plates, as abnormalities.

We address this gap by (1) introducing the first framework that fuses radiographs with demographic metadata, (2) formulating the task as FGVR using transformer-based modeling, and (3) showing that fine-grained pretraining further boosts generalization rather than pretraining on ImageNet.

## 2. METHODS

### 2.1. Dataset Curation & Patient Metadata

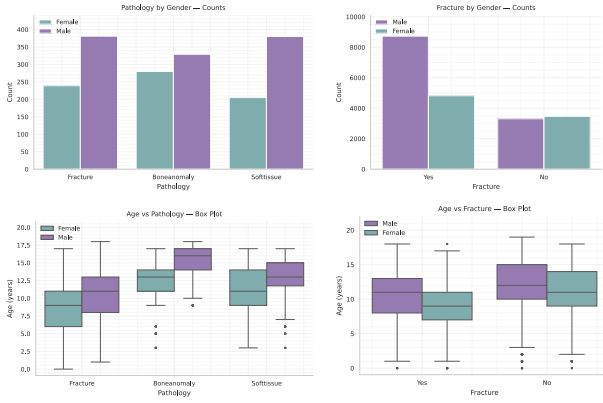
We curated two datasets from GRAZPEDWRI-DX [8]. (1) A “limited” set of three wrist pathologies (fracture, bone anomaly, soft tissue), excluding the “metal” class, following our prior work [9]. (2) A binary “Fracture vs. No Fracture” dataset using all images, with the non-fracture class aug-

**Table 1:** Instances in training, validation, and test sets from the curated datasets.

Three Wrist Pathologies (Limited set)			
Class	Training	Validation	Test
Boneanomaly	392	98	119
Fracture	400	100	120
Soft-tissue	376	94	115
Total	1168	292	354

Fracture vs. No Fracture (Entire set)			
Class	Training	Validation	Test
Fracture	11854	1357	338
No Fracture	10164	1357	338
Total	22018	2714	676



**Fig. 2:** Bar and box plots for gender and age, respectively, for both curated datasets.

mented for balance. Final splits are shown in Table 1. The cohort included 6,091 patients (2,688 female, 3,402 male, ages 0.2–19 years, mean 10.9). Fig. 2 shows distributions: fractures are more common in males, while anomalies concentrate in older groups.

## 2.2. Architectural Details

This work utilizes a hybrid architecture that integrates both visual data and meta-information, drawing inspiration from the MetaFormer architecture [10]. As depicted in Fig. 1, the architecture is organized into five stages. The first stage (S0) starts with a basic 3-layer convolutional stem, which processes raw input images. Subsequent stages progressively downsample the feature maps and increase channel dimensionality. Stages S1 and S2 consist of MBCConv blocks enhanced with squeeze-and-excitation mechanism. The final two stages, S3 and S4, transition to transformer-based blocks that employ relative positional encoding. This design allows the model to capture global dependencies, which are crucial for subtle pathological differences that span larger contexts

**Table 2:** Configuration of the architecture series. B: number of blocks, and H: hidden dimensions for each stage.

Stage	FG-0	FG-1	FG-2
S0	B=3 H=64	B=3 H=64	B=3 H=128
S1	B=2 H=96	B=2 H=96	B=2 H=128
S2	B=3 H=192	B=6 H=192	B=6 H=256
S3	B=5 H=384	B=14 H=384	B=14 H=512
S4	B=2 H=768	B=3 H=768	B=3 H=1024

(e.g., comparing radius vs. ulna contours or detecting diffuse soft tissue swelling).

Downsampling is applied at the beginning of each stage. In S3 and S4, overlapping patch embedding is implemented using convolutions with a stride of 2 and zero-padding, effectively reducing resolution while maintaining contextual overlap. Table 2 outlines the configuration details of the three variants of the architecture used in our experiments.

To overcome the lack of spatial awareness in standard self-attention, the model incorporates a relative position bias. Specifically, a bias matrix  $B \in \mathbb{R}^{((M^2+N) \times (M^2+N))}$  is added during attention computation:

$$\text{Attention}(Q, K, V) = \text{Softmax} \left( \frac{QK^T}{\sqrt{d}} + B \right) V. \quad (1)$$

Here,  $Q$ ,  $K$ , and  $V$  are the query, key, and value matrices of size  $\mathbb{R}^{((M^2+N) \times d)}$ , where  $M^2$  corresponds to the number of image patches and  $N$  is the count of extra tokens (e.g., class and meta tokens). The bias matrix  $\hat{B}$  is parameterized, supporting relative positions from  $-M - 1$  to  $M + 1$ . A shared bias is applied for non-visual tokens since their spatial position is undefined. The Relative Transformer Block comprises multi-head self-attention (MSA), layer normalization (LN), and a multi-layer perceptron (MLP), applied to the input token sequence  $z_0$ :

$$\begin{aligned} z_0 &= [x_{\text{class}}; x_{\text{meta}}^1, \dots, x_{\text{meta}}^{n-1}; x_{\text{vision}}^1, \dots, x_{\text{vision}}^m], \\ z'_i &= \text{MSA}(\text{LN}(z_{i-1})) + z_i, \\ z_i &= \text{MLP}(\text{LN}(z'_i)) + z'_i. \end{aligned} \quad (2)$$

In this formulation,  $z_i \in \mathbb{R}^{(M^2+N) \times d}$  captures the updated token sequence at each transformer layer. Stages S3 and S4 each generate a class token,  $z_{\text{class}}^1$  and  $z_{\text{class}}^2$ , which encode combined visual and meta representations. Since these tokens may differ in dimension,  $z_{\text{class}}^1$  is first projected to match the shape of  $z_{\text{class}}^2$  using an MLP. The two are then concatenated and passed through a 1D convolution followed by normalization:

$$\begin{aligned} \hat{z}_{\text{class}}^1 &= \text{MLP}(\text{LN}(z_{\text{class}}^1)), \\ z_{\text{class}} &= \text{Conv1d}(\text{Concat}(\hat{z}_{\text{class}}^1, z_{\text{class}}^2)), \\ y &= \text{LN}(z_{\text{class}}). \end{aligned} \quad (3)$$

The final output  $y$  aggregates information across multiple scales and token types. When using external attributes as

**Table 3:** Vision-only baselines on the test set. MetaFormer fusion variants (bottom) achieve the best performance.

Model	Accuracy (%) (95% CI)
ViT	59.0 (54.0–64.1)
AlexNet	66.1 (61.3–71.2)
YOLO11s	69.5 (64.7–74.3)
VGG16	70.1 (65.5–74.9)
GoogleNet	72.9 (68.1–77.4)
ResNet50	74.0 (69.8–78.5)
DenseNet201	74.9 (70.3–79.4)
ConvNeXtV2-Tiny	76.0 (71.5–80.2)
InceptionV3	77.1 (72.6–81.4)
Swin Transformer	77.4 (72.9–81.6)
EfficientNetV2	78.0 (73.7–81.9)
<b>MetaFormer (Base)</b>	<b>79.1 (74.9–83.3)</b>
<b>MetaFormer-FG-2-inat-default (Ours)</b>	<b>82.2 (78.2–86.2)</b>
<b>MetaFormer-FG-2-inat-late (Ours)</b>	<b>83.6 (79.7–87.3)</b>

metadata, these are encoded as vectors and embedded using a fully connected non-linear function  $f : \mathbb{R}^n \rightarrow \mathbb{R}^d$ . To prevent overreliance on metadata (and potential overfitting), we apply progressive metadata masking during training, forcing the model to learn robust visual features while still leveraging auxiliary signals.

### 2.3. Experimental Settings

We compare against common CNNs pre-trained on ImageNet [11–21], as shown in Table 3. All models underwent training for 100 epochs using a resolution of  $224 \times 224$  and a batch size of 32. Adam optimizer was utilized with  $lr = 10^{-3}$  for baselines and AdamW with base  $lr = 10^{-4}$  were defaults for MetaFormer.

## 3. RESULTS & DISCUSSION

### 3.1. Baseline Comparison

MetaFormer (vision-only) achieves the highest test accuracy among the compared image-only baselines (Table 3). We quantify uncertainty using 95% bootstrap confidence intervals obtained by resampling test examples with replacement (percentile method,  $B = 2000$ ). Our fusion variants, which incorporate demographic metadata, yield higher accuracy than the vision-only model under the same evaluation protocol.

### 3.2. Ablation Analysis

Integrating demographic metadata (age, sex) consistently improved performance (Table 4). Both early and late fusion surpassed vision-only models, with late fusion achieving the highest gains in two out of three configurations. This finding aligns with the intuition that age and sex provide essential developmental context, particularly relevant in pediatrics, where normal ossification patterns vary across individuals. Late fusion may be more robust to noise in individual modalities, as

combining information at a later stage allows the final decision to benefit from multiple sources, potentially mitigating the impact of noise or errors in any single modality.

Attribute-level analysis (Table 5) further indicates that both age and sex independently contribute to performance, but their combination yields the largest benefit, supporting the clinical relevance of demographic context.

We then selected the “FG-2” configuration and used the weights obtained from training it on the iNaturalist dataset [22] to create our “FG-2-inat” configuration. This surpassed all other configurations, whether using image data alone or in conjunction with metadata. This configuration reached 81.4%, a 1.5% improvement over image-only training. It seems that the fine-grained pretraining improved generalization beyond ImageNet pretraining, reflecting the value of transferring from domains where subtle inter-class variations dominate.

**Table 4:** Joint evaluation of architecture configuration and fusion strategy reported with test accuracy (%) (95% CI).

Config	Vision	Late Fusion	Early Fusion	Default Fusion
FG-0	79.1 (74.9–83.3)	79.4 (75.1–83.3)	75.1 (70.6–79.7)	78.5 (74.0–82.5)
FG-1	77.4 (73.2–81.6)	78.0 (73.4–82.2)	<b>76.0 (71.5–80.2)</b>	79.7 (75.4–83.6)
FG-2	78.5 (74.3–82.5)	80.5 (76.3–84.5)	74.9 (70.3–79.4)	73.4 (68.6–78.0)
<b>FG-2-inat (Ours)</b>	<b>82.2 (78.2–86.2)</b>	<b>83.6 (79.7–87.3)</b>	75.1 (70.6–79.7)	<b>82.2 (78.2–86.2)</b>

**Table 5:** Accuracies obtained by FG-2-inat-default configuration on metadata attributes.

Attribute	Accuracy (%) (95% CI)
Vision + Age	79.7 (75.4–83.6)
Vision + Gender	79.1 (74.9–83.3)
Vision + Age + Gender	82.2 (78.2–86.2)
Vision + Age + Gender (late-fusion)	<b>83.6 (79.7–87.3)</b>

**Table 6:** Effect of masking schedule and probability on test accuracy.

Mask Type	Mask Prob	Accuracy (%) (95% CI)
Constant	0.1	79.7 (75.4–83.9)
	0.2	79.1 (75.1–83.3)
	0.3	79.7 (75.1–83.6)
	0.5	79.4 (75.1–83.3)
Linear	0.1	79.7 (75.4–83.6)
	0.2	78.8 (74.6–83.1)
	0.3	78.8 (74.6–83.1)
	0.5	79.4 (75.1–83.6)
<b>Progressive (Ours)</b>	Scheduled	<b>82.2 (78.2–86.2)</b>

Too little masking encourages overreliance on metadata (hurting robustness), while too much/constant masking prevents the model from exploiting useful auxiliary cues; the default progressive schedule best balances these.

**Table 8:** Performance evaluation on a significantly larger (fracture vs. no fracture) dataset.

FG-2-inat (Ours)	Test Accuracy (%)
Vision Only	50.1
Vision + Meta	<b>60.4</b>

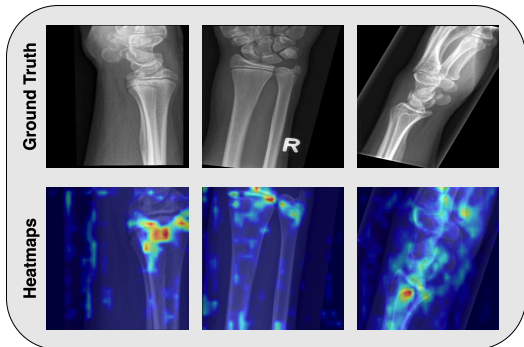


**Fig. 3:** Heatmaps from the final convolutional layer in stage 2 (S2) of our configuration “FG-2-inat” on a limited dataset.

### 3.3. Interpretability & diagnostic performance analysis

GradCAM heatmaps (Fig. 3) demonstrate that MetaFormer attends to clinically relevant wrist regions, particularly around fracture lines and anomalous bone structures. While most heatmaps align well with pathology, some exhibit diffuse attention, suggesting occasional reliance on spurious features. This indicates that while metadata integration improves classification, further refinement is needed for precise localization. Nevertheless, the alignment of salient regions with clinical expectations strengthens confidence in the model’s decision process. Table 7 shows per-class sensitivity, specificity, & precision scores for configuration “FG-2-inat”. Similarly, as shown in Fig. 4, metadata enhances fracture detection while preserving performance in bone anomaly and soft tissue recognition.

**Table 7:** Evaluation of our default fusion (FG-2-inat).

Configuration	Cls	Sensitivity (%)	Specificity (%)	Precision (%)
Vision Only	0	62.2	98.7	96.1
	1	100.0	82.9	75.0
	2	77.4	88.3	76.1
Vision+Meta	0	66.4	98.7	96.3
	1	100.0	82.9	75.0
	2	77.4	90.4	79.5

On the larger “Fracture vs. No Fracture” dataset (Table 8), metadata integration produced a 10% absolute gain, underscoring the robustness of multimodal learning even when the task is coarser. These results suggest that metadata not only aids fine-grained wrist pathology recognition but also enhances scalability to larger clinical datasets.

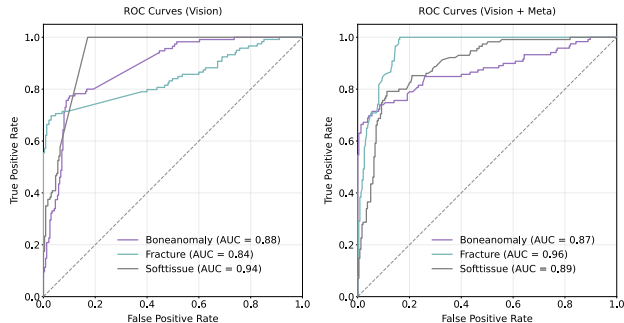


**Fig. 4:** ROC curves showing that metadata substantially improves fracture discrimination (AUC 0.84→0.96).

### 3.4. Failure cases & error analysis

On the held-out test set (n=354), most errors arise from confusions between class 0→2 (25 cases) and class 2→1 (23 cases), with class 0 showing high precision (0.96) but lower recall (0.66), suggesting that subtle/no-fracture cases are sometimes overcalled as more severe findings. We also observe a mild performance drop for older age bins ( $\approx 0.75$ – $0.77$  accuracy for age\_norm  $\geq 0.526$  vs  $\approx 0.91$  for age\_norm  $< 0.526$ ), consistent with increased anatomical variability and ossification-related appearance changes. Performance is comparable across sex. Finally, a subset of correct predictions has low confidence (median confidence  $\approx 0.74$  overall), indicating borderline cases where the model is uncertain and may benefit from clinician review.

## 4. CONCLUSION

Overall, our experiments demonstrate three key findings: (1) Fine-grained transformer architecture outperforms conventional CNNs for pediatric wrist pathology. (2) Demographic metadata (age, sex) significantly improves recognition across both limited and large-scale datasets, with late fusion being most effective. (3) Fine-grained pretraining enhances generalization compared to using ImageNet weights. These results emphasize that integrating developmental context into vision models is essential for robust pediatric musculoskeletal diagnosis.

## 5. ACKNOWLEDGEMENT

This work was supported by the CONNECT Project NORPART-2021/10502, funded by the Norwegian Directorate for Higher Education and Skills (DIKU).

## 6. REFERENCES

- [1] Bryan C. MD Hoynak, “Wrist Fracture Management in the ED,” Practice Essentials, Pathophysiology, Prognosis, 2022.
- [2] Spencer A. Thomas, “Combining Image Features and Patient Metadata to Enhance Transfer Learning,” in *2021 43rd Annual International Conference of the IEEE Engineering in Medicine and Biology Society (EMBC)*, 2021, pp. 2660–2663.
- [3] Gan Cai, Yu Zhu, Yue Wu, Xiaoben Jiang, Jiongyao Ye, and Dawei Yang, “A Multimodal Transformer to Fuse Images and Metadata for Skin Disease Classification,” *The Visual Computer*, vol. 39, no. 7, pp. 2781–2793, 2023.
- [4] Florian Hinterwimmer, Michael Guenther, Sarah Consalvo, Jan Neumann, Alexandra Gersing, Klaus Woertler, Rüdiger von Eisenhart-Rothe, Rainer Burgkart, and Daniel Rueckert, “Impact of metadata in multimodal classification of bone tumours,” *BMC Musculoskeletal Disorders*, vol. 25, no. 1, Oct 2024.
- [5] Namazi H;Khaje R, “Normal age-related alterations on distal radius radiography,” *The archives of bone and joint surgery*, vol. 3, no. 4, 2015.
- [6] Ki Yap, Craig Hacking, and Jeremy Jones, “Ossification centres of the wrist,” *Radiopaedia.org*, Nov 2010.
- [7] Karen Rosendahl, Ramona Myklebust, Kjersti Foros Ulriksen, A. Nøttveit, Pernille Eide, Åsmund Djuve, and Christina Brudvik, “Incidence, pattern and mechanisms of injuries and fractures in children under two years of age,” *BMC Musculoskeletal Disorders*, vol. 22, no. 1, Jun 2021.
- [8] Eszter Nagy, Michael Janisch, Franko Hržić, Erich Sorantin, and Sebastian Tschauner, “A pediatric wrist trauma x-ray dataset (grazpedwri-dx) for machine learning,” *Nature News*, 2022.
- [9] Ammar Ahmed, Ali Shariq Imran, Zenun Kastrati, Sher Muhammad Daudpota, Mohib Ullah, and Waheed Noor, “Learning from the few: Fine-grained approach to pediatric wrist pathology recognition on a limited dataset,” *Computers in Biology and Medicine*, vol. 181, pp. 109044, 2024.
- [10] Qishuai Diao, Yi Jiang, Bin Wen, Jia Sun, and Zehuan Yuan, “MetaFormer: A Unified Meta Framework for Fine-Grained Recognition,” *arXiv.org*, 2022.
- [11] Jia Deng, Wei Dong, Richard Socher, Li-Jia Li, Kai Li, and Li Fei-Fei, “Imagenet: A large-scale hierarchical image database,” in *Proceedings of the IEEE Conference on Computer Vision and Pattern Recognition (CVPR)*. IEEE, 2009, pp. 248–255.
- [12] Alexey Dosovitskiy, Lucas Beyer, Alexander Kolesnikov, Dirk Weissenborn, Xiaohua Zhai, Thomas Unterthiner, Mostafa Dehghani, Matthias Minderer, Georg Heigold, Sylvain Gelly, Jakob Uszkoreit, and Neil Houlsby, “An Image is Worth 16x16 Words: Transformers for Image Recognition at Scale,” 2020.
- [13] Karen Simonyan and Andrew Zisserman, “Very Deep Convolutional Networks for Large-Scale Image Recognition,” 2015.
- [14] Christian Szegedy, Wei Liu, Yangqing Jia, Pierre Sermanet, Scott Reed, Dragomir Anguelov, Dumitru Erhan, Vincent Vanhoucke, and Andrew Rabinovich, “Going Deeper with Convolutions,” 2014.
- [15] Mingxing Tan and Quoc V. Le, “EfficientNetV2: Smaller Models and Faster Training,” 2021.
- [16] Alex Krizhevsky, Ilya Sutskever, and Geoffrey E. Hinton, “ImageNet Classification with Deep Convolutional Neural Networks,” in *Advances in Neural Information Processing Systems*. 2012.
- [17] Gao Huang, Zhuang Liu, Laurens van der Maaten, and Kilian Q. Weinberger, “Densely Connected Convolutional Networks,” 2018.
- [18] Christian Szegedy, Wei Liu, Yangqing Jia, Pierre Sermanet, Scott Reed, Dragomir Anguelov, Dumitru Erhan, Vincent Vanhoucke, and Andrew Rabinovich, “Going deeper with convolutions,” in *2015 IEEE Conference on Computer Vision and Pattern Recognition (CVPR)*. IEEE, 2015, pp. 1–9.
- [19] Kaiming He, Xiangyu Zhang, Shaoqing Ren, and Jian Sun, “Deep Residual Learning for Image Recognition,” 2015.
- [20] Sanghyun Woo, Shoubhik Debnath, Ronghang Hu, Xinlei Chen, Zhuang Liu, In So Kweon, and Saining Xie, “Convnext v2: Co-designing and scaling convnets with masked autoencoders,” 2023.
- [21] Ze Liu, Yutong Lin, Yue Cao, Han Hu, Yixuan Wei, Zheng Zhang, Stephen Lin, and Baining Guo, “Swin Transformer: Hierarchical Vision Transformer using Shifted Windows,” *arXiv preprint*, 3 2021, arXiv:2103.14030.
- [22] Grant Van Horn, Oisín Mac Aodha, Yang Song, Yin Cui, Chen Sun, Alex Shepard, Hartwig Adam, Pietro Perona, and Serge Belongie, “The iNaturalist Species Classification and Detection Dataset,” *arXiv.org*, April 2018.